The role of dynamic recrystallization in [001] single-crystal W and W-Ta alloy ballistic rod penetration into steel targets

C. PIZAÑA, E. V. ESQUIVEL, L. E. MURR*, C. Y. PIÑA, M. T. BAQUERA,
I. A. ANCHONDO
Department of Metallurgical and Materials Engineering, The University of Texas at El Paso, El Paso, TX 79968, USA
E-mail: fekberg@utep.edu

L. S. MAGNESS
U.S. Army Research Laboratory, Aberdeen Proving Ground, MD 21005, USA

The microstructures of long rod [001] single-crystal penetrators of W grown by CVD and zone melt processing, and W-5% Ta grown by zone melt (ZM) processing, were examined before and after penetration into RHA steel targets, by optical metallography and transmission electron microscopy. The initial Vickers microhardness values for the CVD-W rods was 417 VHN in contrast to 485 VHN for the ZM-W and W-5% Ta rods as a consequence of an order of magnitude larger dislocation density. Both the CVD-W and ZM-W exhibited less dense head flow associated with adiabatic shear bands and dynamic recrystallization (DRX) than the ZM-W-5% Ta, but all penetrators exhibited erosion tube formation in the penetration channel. These tube and erosion debris particles exhibited dense, overlapping shear bands composed of DRX grains or areas with larger, equiaxed grains resulting from residual grain growth. These observations suggest that controlling the penetrator head flow by solute-induced DRX may control penetration.
© *2005 Springer Science + Business Media, Inc.*

1. Introduction

There is now overwhelming evidence that super-plastic flow facilitated by dynamic recrystallization (DRX) provides the mechanism for extreme deformation, especially high-strain rate deformation of crystalline and polycrystalline metals and alloys [1–8]. The most obvious deformation modes include ballistic impact and penetration where both the projectile and target flow in the solid state [3, 9], hypervelocity impact, explosive welding [10], and friction welding; specifically friction-stir welding [2, 7]. High-density kinetic energy (rod) ballistic penetrators have been a particular focus of dynamic-recrystallization-induced flow phenomena studies. Such high-density ballistic rods include, oriented W columnar-grained rods [4, 7, 8], W single crystal [001] rods, W-4% Ta [001] single-crystal rods [6–8], and tungsten heavy alloy (WHA) (93% W in a 5% Ni + 2% Fe metal matrix) sintered rods [6–8]. In a recent comparative study of tungsten and tungsten-alloy ballistic penetrator rods, Esquivel *et al.* [8] demonstrated that adiabatic shear bands promoting rod deformation and penetration were composed of dynamically recrystallized grains and grain regimes. Furthermore,

Esquivel *et al.* [8] concluded that the DRX grains not only facilitated the solid-state flow, but could ultimately increase rod penetration, if strategies promoting shear band optimization were implemented.

Earlier, Magness [11] proposed that the greater penetration of depleted uranium (DU: U-0.75 Ti or U-6 Nb for example), with densities ranging between $\sim$18 to 19 Mg/m^3 (g/cm^3), in contrast to single-crystal [001] oriented W, with a density of $\sim$19.3 Mg/m^3, was due to failure-mode differences and profuse adiabatic shear banding in the DU; where the DU was polycrystalline. Efforts to emulate the DU rod penetrator behavior, with W and W-alloy single-crystal penetrators, have been neither consistent nor particularly successful. The exceptional penetration depth of [001] oriented W rods featured in the hallmark work by Bruchey *et al.* [12] and Kingman and Herring [13] has not been successfully duplicated. Despite the inability to completely replicate Bruchey's results, the reverse ballistic tests of Leonard *et al.* [14] on oriented, columnar-grained W demonstrated a roughly 41% greater penetration into rolled homogeneous armor steel (RHA: MILA-12560, Class 3 steel) for [001] rods in contrast to [110] and

[111] rods. By comparison, identical DU kinetic energy (K.E.) rod penetrators exhibited a 25% greater penetration into RHA than the columnar, [001] W rod penetrators in this same test series [14].

Furthermore Grace [15] has shown that the penetration of long K.E. rods at impact velocities > 0.5 km/s is characterized by simultaneous rod and target erosion in conjunction with rod deceleration and target acceleration. In effect this means, as has been observed experimentally [6–9], that both the penetrating rod and the target flow are dominated by DRX-assisted solid-state processes. As the penetrating rod head material flows back along the penetrated target channel wall, it effectively forms a tube of DRX material. While the strategy to improve rod penetration into a target must include the production of adiabatic shear bands and shear band structures dominated by DRX, there must also be some form of flow optimization which is currently not well understood.

In the present study, the microstructures of several different [001] oriented single-crystal rod penetrators and penetrator fragments in RHA targets were examined and compared by optical metallography (OM) and transmission electron microscopy (TEM). These rods included two zone-melt (ZM)-produced single crystals of W and W-5% Ta, and three W [001] single crystals produced by chemical vapor deposition (CVD). The aim of this study was to confirm prior observations of microstructural features, particularly DRX occurrence, and to further assess the role of DRX in the rod penetration process.

2. Experimental

Rod penetrator fragments of [001] oriented single-crystal tungsten and tungsten-tantalum produced by ZM and CVD were studied. Both W and W-5% Ta ZM single-crystal rods were produced by drawing from the melt in the [001] orientation. All other W single crystal rods were grown homoepitaxially by CVD to the required rod diameter. These were all machined to hemi-nosed rods with a length over diameter ratio of approximately 15 (l/d~15) by General Atomics, Inc. (USA). The rods were subsequently launched at the Army Research Laboratory (ARL) in Aberdeen, MD into RHA (MIL-A-12560 steel) thick targets at nominal velocities ranging from 1.2 to 1.4 km/s using a gun breech assembly with a custom made 40 mm smoothbore barrel. The gun was positioned approximately 3 m in front of the targets and the propellant weight adjusted to achieve the desired velocities. Striking and residual velocities along with orientation and mass of the penetrator rods were recorded and documented. Table I depicts the information characterizing the experimental penetrator fragments. Penetrator head fragments and erosion debris were characterized by location preceding the penetration or impact, i.e. penetrator head and/or penetrator tube. The tube notation refers to the penetrator erosion debris which can flow from the head of the penetrator and create a somewhat contiguous, cylindrical tube or tube-like fragment in the penetration channel wall.

All samples were cut longitudinally and transversely, polished and etched with equal amounts of H_2O, 3%

TABLE I Experimental penetrator data

Shot ID	Growth method and material	Orientation	Samples (sample type)	Striking velocity (m/s)	Residual velocity (m/s)
4643	Zone-Melt W	[001]	Residual penetrator	1338	580*
4644	Zone-Melt W	[001]	Residual penetrator	1320	445*
1	CVD W	[001]	Residual penetrator	1254	5 mm bulge
2	CVD W	[001]	Residual tube	1367	461*
3	CVD W	[001]	Residual tube	1303	526*
4	Zone-Melt W-5% Ta	[001]	Residual Penetrator	1307	7 mm bulge

*Residual velocity is indicative of an exit velocity for the penetrator. Those indicated by a bulge size represent targets too thick to penetrate, and the penetrator head was left in the target.

H_2O_2, and NH_4OH. Optical metallography was performed with a Reichert MEF4 A/M optical microscope. Vickers microhardness measurements were made with a Shimadzu HMV-2000 microhardness tester using a standard diamond indenter at a 100gf (1N) load for 10s. These measurements were made over embedded, polished fragment surfaces to create maps of residual micro-hardness, recorded in Vickers hardness number (VHN) notation; 1 VHN = 0.01 GPa.

Samples of the original rod bar stock and penetrator fragments and debris were also prepared for transmission electron microscopy (TEM). The electro-polishing was performed on a Tenupol-3 twin jet polisher using a solution of 750 mL methyl alcohol, 350 mL ethyl alcohol, 150 mL glycerol, 135 mL H_2SO_4 and 75 mL HF. The samples were examined in a Hitachi H-8000 transmission electron microscope at an accelerating voltage of 200 kV, utilizing a goniometer-tilt stage. Samples were also examined by scanning electron microscopy (SEM) (ISI-DS-130) prior to optical metallography and the cutting and polishing required for TEM.

3. Results and discussion

Fig. 1 shows a composite of photographic views of the original single-crystal penetrator rods or rod segments and TEM views of traverse slices from these rod segments. Macro photographs of the [001] oriented single-crystals in their original, as grown state, are shown in Figs 1a and b. Figs 1c, d and e illustrate the original, pre-penetrator dislocation microstructure in transverse [001] sections for the CVD-W, ZM-W and ZM-W-5%-Ta rods respectively. For comparison Figs 2a to c show the corresponding dislocation substructures and recovered and DRX grain microstructures of post-penetration fragments observed in the target. Fig. 2 provides evidence of residual recovery (Fig. 2a), heavy deformation (Fig. 2b), and/or dynamic recrystallization (Fig. 2c) which occurred during the penetration process in contrast to the lower dislocation density observed in the initial single-crystal rods (Fig. 1). Although starting dislocation microstructures observed in both CVD and ZM formed rods were similar (ranging from 10^8 to 10^9 cm^{-2} for the CVD-W and the ZM rods,
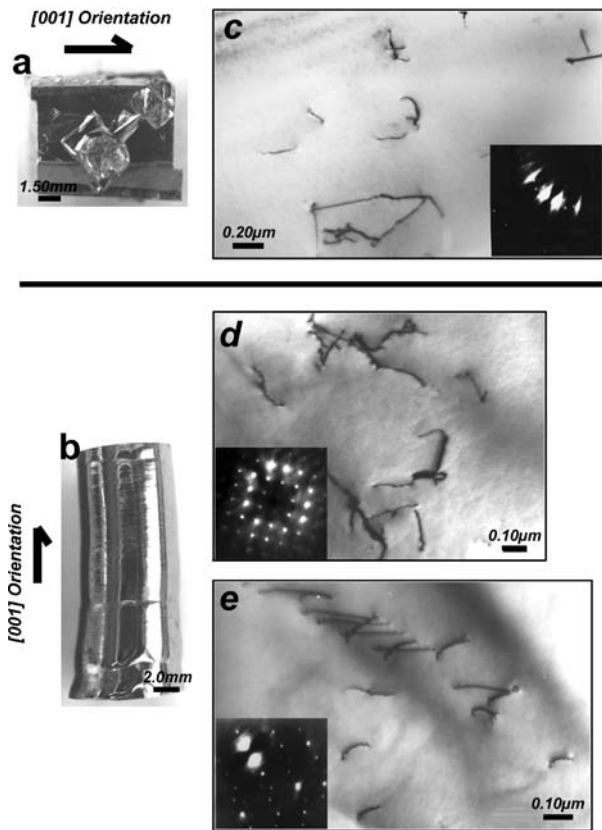
Figure 1 TEM images of starting rod microstructures and their respective pre-machined projectiles. (a) Pre-machined (as grown) CVD formed single-crystal W showing [001] orientation. (b) Pre-machined (as grown) ZM formed single-crystal W showing [001] orientation. (c) [001] transverse section for CVD formed single-crystal W. (d) [001] transverse section for ZM formed single W. (e) [001] transverse section for ZM single-crystal W-5%Ta.

Figure 2 TEM images of residual rod microstructures and their corresponding diffraction patterns. (a) Single-crystal CVD formed W rod fragment after penetration. (b) Single-crystal ZM formed W-rod fragment after penetration. (c) W-5%Ta single-crystal ZM formed rod fragment after penetration. The diffraction patterns in (a) and (c) show polycrystallinity.

respectively) Vickers microhardness measurements revealed a difference in hardness between the two rod growth methods (i.e. CVD and ZM). An average Vickers microhardness number (VHN) value of 417 was obtained for the CVD rods as compared to 486 VHN for the ZM rods; consistent with a somewhat higher dislocation density in the CVD materials noted. The initial RHA steel target microhardness was observed to be relatively softer than the penetrators at an average of 339 VHN.

Fig. 3 shows a somewhat exaggerated schematic (cartoon) illustrating the principal features of K.E. rod penetration into a thick steel target. As the rod penetrates, material is eroded from the rod head by DRX-assisted flow which produces an erosion tube of flowing debris against the penetration channel wall. The penetrated target material flows outward and opposite to the penetrating rod, forming a crater rim at the entrance where material can be ejected by jetting and particulation. As the rod is eroded by DRX flow, extending the erosion channel, its mass is consumed. Behind the flow regime of the rod head there is a regime of blocky, cleavage fracture which can produce larger debris fragments within the flow regime of the eroding rod. Behind this zone heavy deformation, indicated by deformation twinning, can be observed [4, 8]. The residual samples examined in this research program as illustrated in the comparative TEM views of Fig. 2, and listed in Table I, can be associated with the erosion debris fragments composing
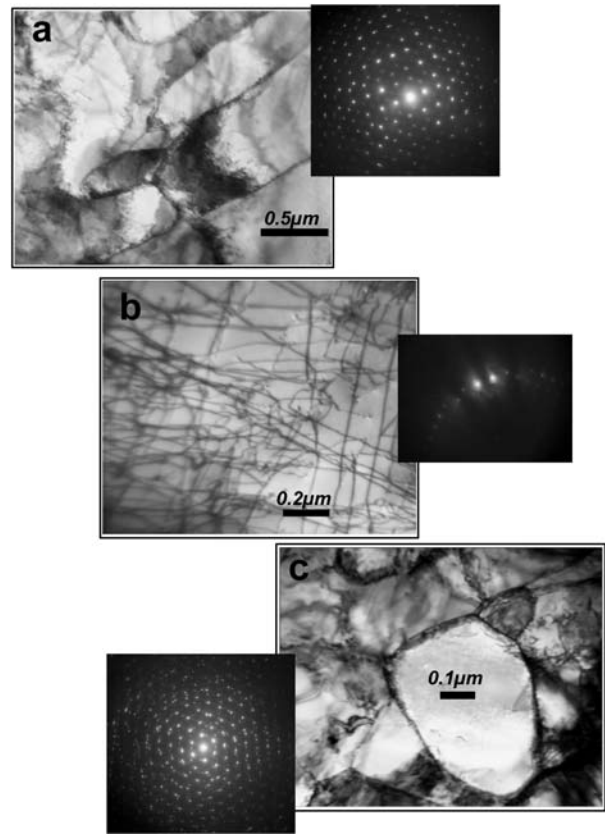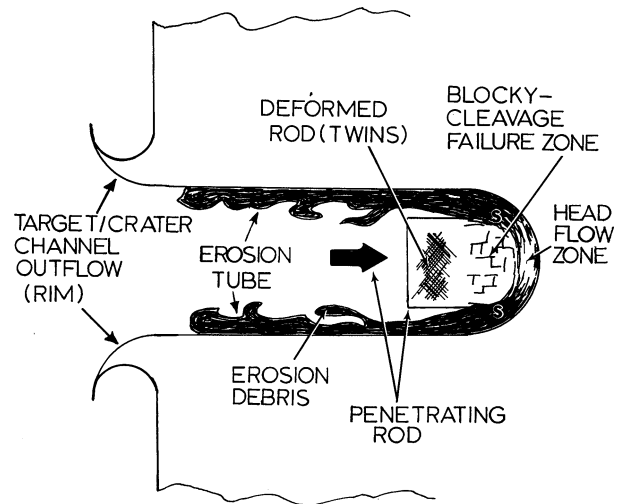

Figure 3 Schematic (cartoon) view of K.E. rod penetration into a thick (steel) target. s denotes the nucleation of shear bands which allow for solid state flow and erosion of the rod head forming an erosion tube shown.

the residual (erosion) tube, more nearly intact, residual penetrator heads, or head fragments.

3.1. CVD formed W, [001] oriented single crystal residual fragments

Fig. 4a illustrates an optical cross-section view (in dark-field) of a recovered CVD-formed, residual tube fragment with head-like features obtained from shot ID #3
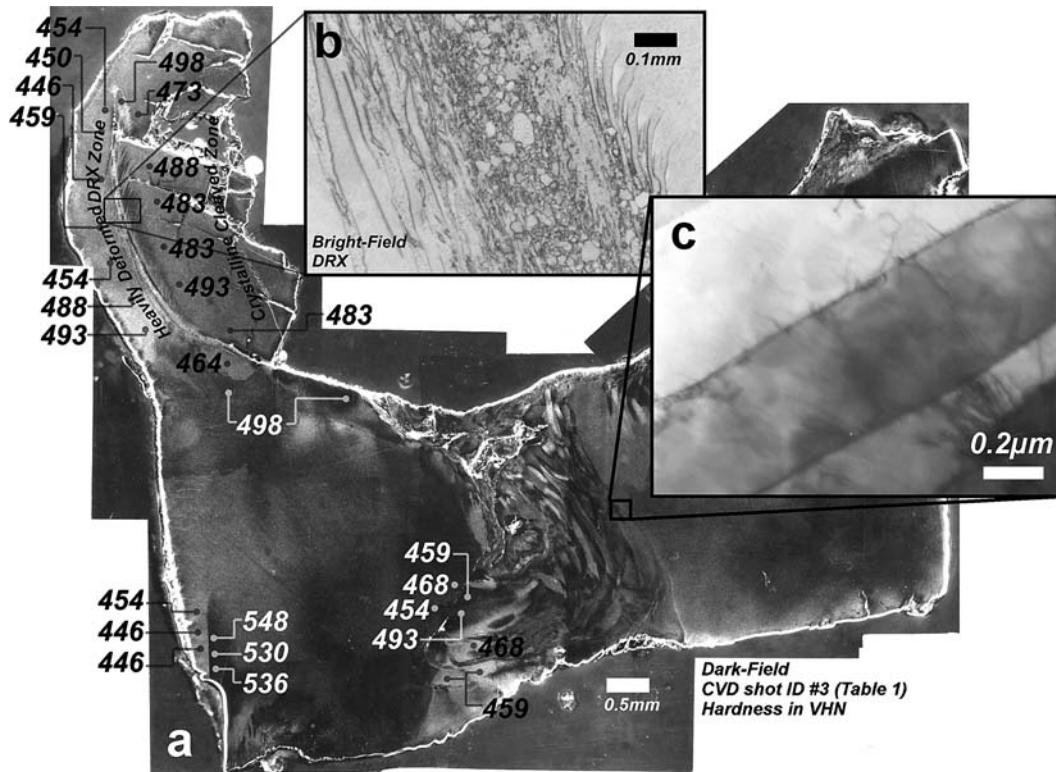
Figure 4 Cross-section view in dark-field of a residual frament obtained from shot ID# 3 (Table I) after penetration showing Vickers microhardness numbers (VHN) (a). (b) Magnified view of shear band composed of DRX grains. (c) TEM image obtained from a transverse thin section at location shown.

(Table I) after penetration. Although the sample was characterized as a residual tube fragment (Fig. 3) in Table I, the flow features which are particularly located on the top left section of the fragment in Fig. 4a are characteristic of residual head fragments; especially near the shear initiation zones noted "s" in Fig. 3. Such features include the wide DRX shear band (Fig. 4b) which divides part of the fragment into two regimes: the outer flow regime to the left, and the cleavage or blocky zone to the right (Fig. 3). The two distinct zones in Fig. 4a which not only differ in optical (contrast) appearance but also in residual microhardness as well, provide evidence of an erosion and/or transfer process characteristic of penetration, specifically penetration found at or near the head of the penetrator. The VHN values obtained between the two sides of the shear band (Fig. 4b) can be observed to average 463 VHN on the left hand side of the band while the right hand side averaged 485 VHN. The softer material (463 VHN), which is consistently located near the head surface (~0.5 mm thick), is probably part of the erosion regime. Evidently this softer region must undergone some deformation and/or dynamic recrystallization to eventually form a microstructure that is harder (463 VHN) than the original single-crystal structure (417 VHN) and yet softer than the cleaved zone present in the same fragment. On the other hand, this latter, harder side of the shear band (cleaved side), which averaged a microhardness value of 485 VHN, also suggests heavy deformation, although either at a much higher degree (more than the softer side) and/or representing a lack of dynamic recrystallization. Furthermore, given that the original material is not only softer but also cleaves in specific crys-

tallographic directions, this zone is thought to consist of crystalline, heavily deformed blocks. Flow therefore, could be accommodated by thin DRX zones formed between the crystalline blocks.

While the shear zone shown enlarged in Fig. 4b illustrates DRX and grain growth producing an intermixing of grain sizes ranging from <5 to ~50 μm, other regions show similar recovery microstructures and DRX zones as illustrated in the magnified TEM view shown in Fig. 4c. Other regions showing microhardness anomalies in Fig. 4, such as the 548 VHN value shown in the lower left portion of Fig. 4, are indicative of other deformation features.

A further examination of the shear band/flow regime in Fig. 4b reveals crystallographic features bending and merging from both sides, into the band. Opposing sides marked L (*left side*) and R (*right side*) in Fig. 5a, illustrate different types of flow-produced crystallographic characteristics as indicated by the arrows in Fig. 5c, which reproduces the enlargement of Fig. 4b. On the right hand side, the crystallographic features appear to be elongated, thin and are consistently located at and beyond the rim of the band. In contrast, on the left hand side, these characteristics appear to be much shorter, thicker and are located solely at the rim of the band. Both of these are consistent with prior findings of Pappu *et al.* [4] who describe these characteristics as linear deformation features, including lenticular-like, linear microstructures which were later confirmed to be Neumann bands (or deformation twins).

Within the band in Fig. 5a DRX grain structure is predominantly equiaxed, with both large and small grains appearing throughout the band as seen in the magnified
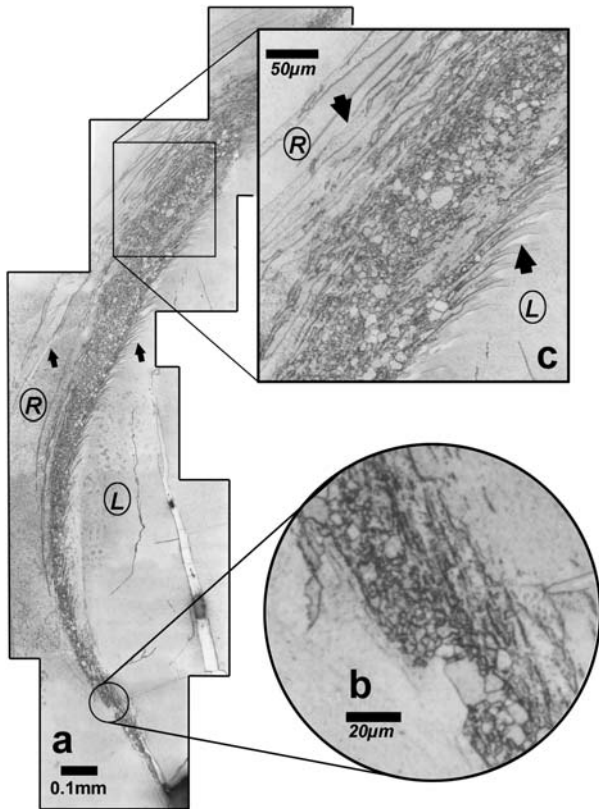
Figure 5 Cross-section view of shear band composed of DRX grains obtained from shot ID#3 (Table I). (a) L and R indicating distinct zones on respective sides of the shear band. (b) Magnified view showing DRX grain structure at a thinner band section. (c) Magnified view showing equiaxed DRX grain structure at a thicker band section. Arrows indicating distinct flow-induced features along both sides of the shear band.

Figure 6 CVD-formed residual W tube fragment obtained from shot ID#2 (Table I) after penetration. (a) Macro-graph of residual tube fragment obtained after penetration from shot ID #2 (Table I). (b) Magnified cross-section view of the tube fragment showing Vickers microhardness numbers (VHN). (c) Magnified view of cross-section showing flow zone composed of DRX material and shear bands. Arrow indicating overlapping microshear bands. The large arrow indicating "rod flow" is indicative of the rod (penetration) axis shown by the large arrow in Fig. 3.

views in Figs 5b and c, and as noted previously. As described by Esquivel *et al.* [8] in a comparative study between columnar grain W and single-crystal W-4%Ta, the adiabatic shear band functions as a type of microstructural lubricant that provides the mechanism and vehicle for erosion and/or transfer of material from the penetrator head to the tube (Fig. 3). Other optical features as well as TEM images shown in Fig. 4c seem to support the notion that the penetrator flows due to DRX during the penetration process, specifically in the tube and head surface regions of the fragment.

The current strategy to improve rod penetration into a target, suggested by Esquivel *et al.* [8], must take into account the optimized production and/or control of such adiabatic shear bands, and shear band structures dominated by DRX. While the overall flow and penetration of the projectile depends on shear bands, inherently, the shear bands themselves diminish the overall mass by promoting projectile erosion and inhibiting target erosion. Erosion in both target and penetrator needs to be optimized in order to increase flow of the penetrating projectile, while at the same time reducing the amount of material being eroded from it.

Figs 6 and 7 (obtained from fragments of shot ID #2, Table 1) illustrate excellent examples of the erosion tube (Fig. 3) created from [001] oriented, CVD-W penetrators as a consequence of solid-state flow. Although the cross-section view in Fig. 6a might be confused wi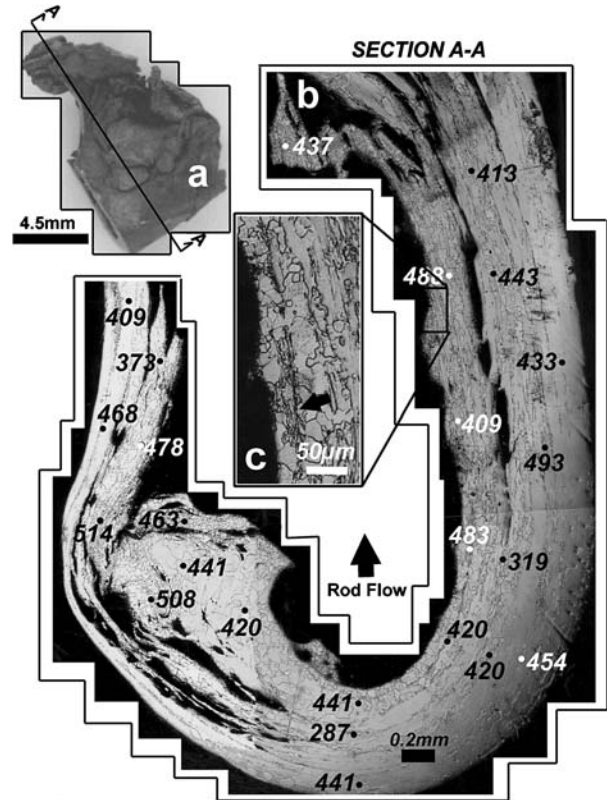th that of a penetrator head, the figure illustrates a residual tube section that evidently folded onto itself during and/or after penetration, as shown schematically in Fig. 3. Both Figs 6b and 7a reveal overlapping shear bands which ultimately compose the flow zones as denoted by the arrows in Figs 6c and 7c. Figs 6c and 7b provide further evidence of the propensity for the erosion tube segments to completely recrystallize and form large, equiaxed grain structures, as a result of grain growth during penetration.

The microhardness mappings throughout the debris fragments shown in Figs 6 and 7 show variations in softening and hardening relative to the initial CVD-W [001] rod hardness of 417 VHN: for example readings in the erosion tube segment shown in Fig. 6 range from a low of 287 VHN to a high of 508 VHN.

3.2. ZM formed W [001] oriented single-crystal residual fragments

Fig. 8a illustrates a W, ZM-formed residual rod head and erosion tube fragment obtained from shot ID #4643 (Table I) after penetration (Fig. 3). Section A-A in Fig. 8a is a cross-section of the fragment taken at approximately half the diameter of the head (Fig. 8b). Similar to the CVD-W fragments, Fig. 8b reveals well-defined areas of cleaved, blocky, and heavily deformed DRX material including well defined zones where overlapping shear (flow) bands exist (Fig. 3). The initial,
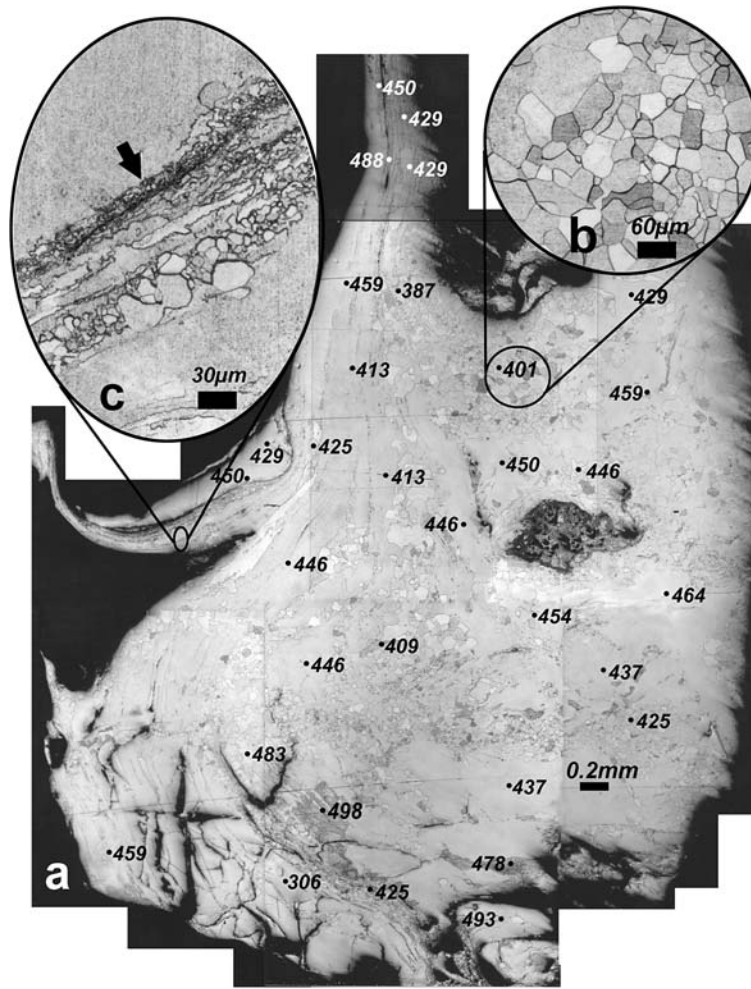
Figure 7 Magnified cross-section view of a residual CVD-W tube fragment and Vickers microhardness map showing VHN values at locations in (a). (b) Magnified view of cross-section showing zone composed of essentially equiaxed, large, DRX grains. (c) Magnified view of cross-section showing a flow zone composed of overlapping shear bands and DRX grains. Arrow indicating overlapping shear bands.
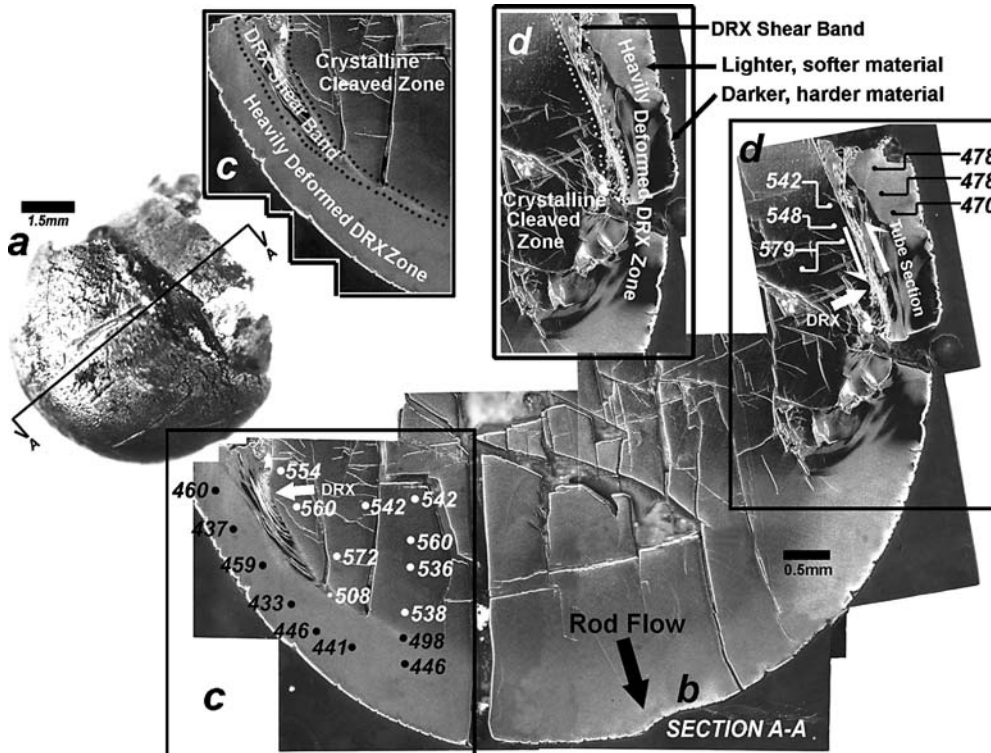

Figure 8 Macrograph of a ZM-W formed residual head fragment obtained from shot ID#4643 (Table I) after penetration (a). (b) Cross-section view of the fragment and Vickers microhardness map showing VHN values in sections c and d. (e) Section c depicting zones of heavily deformed DRX material and cleaved material. (f) Section d depicting zones of heavily deformed DRX material and cleaved material.

as-grown ZM-W [001] oriented rod Vickers microhardness average value of 486 VHN can be compared with the softer, average value of 446 VHN in Fig. 8c. The heavily deformed DRX zone found at the surface of the projectile after penetration suggests that the initial shock compression and penetration deformed and ultimately dynamically recrystallized the surface of the head. Consequently, the penetrator appears to flow through the target facilitated by a surface zone composed of DRX and/or heavily deformed material. Note the arrow in the lower rendition of Figs 8c and d which shows shear band nucleation at the outer regions of the rod head between the blocky/cleavage of regime and the material flowing into the erosion tube as shown schematically in Fig. 3 at "s".

Moreover, and also consistent with the CVD fragment described earlier in Figs 4 to 7, the harder (549 VHN) cleaved region, is reliably located near the embedded rod head center and probably flows as large, heavily deformed crystalline blocks on thin DRX boundaries as noted previously.

The two distinct zones labeled, "Heavily Deformed DRX Zone" and "Crystalline Cleaved Zone", in Figs 8c and d are divided by conspicuous adiabatic shear bands characterized by dynamic recrystallization. The location of such bands in reference to the penetrator head (peripherally on both sides of the head as shown by "s" in Fig. 3) indicates that the major flow activity (erosion from head to tube) might occur at distinct locations within the penetrator. These zones indicated by arrows in Fig. 8b illustrate larger recrystallized grains which might be indicative of a highly localized strain region.

A small tube section which is labeled in Fig. 8c, appears to be on the verge of separating from the bulk of the penetrator head, probably due to shear along the penetrated channel wall. Flow features within the tube seem to suggest that the tube is formed by a thin surface along the head of the penetrator which is strained along the flow of the penetrating head. The softer, optically lighter region depicted in Fig. 8d suggests DRX, as compared to the darker, harder regions which are indicative of a heavily deformed, crystalline structure. Both of these types of material microstructures seem to interact as flow features and ultimately merge into the DRX shear band. The band provides the so called lubrication in order for the tube and head section to shear away from each in the direction illustrated in Fig. 8d.
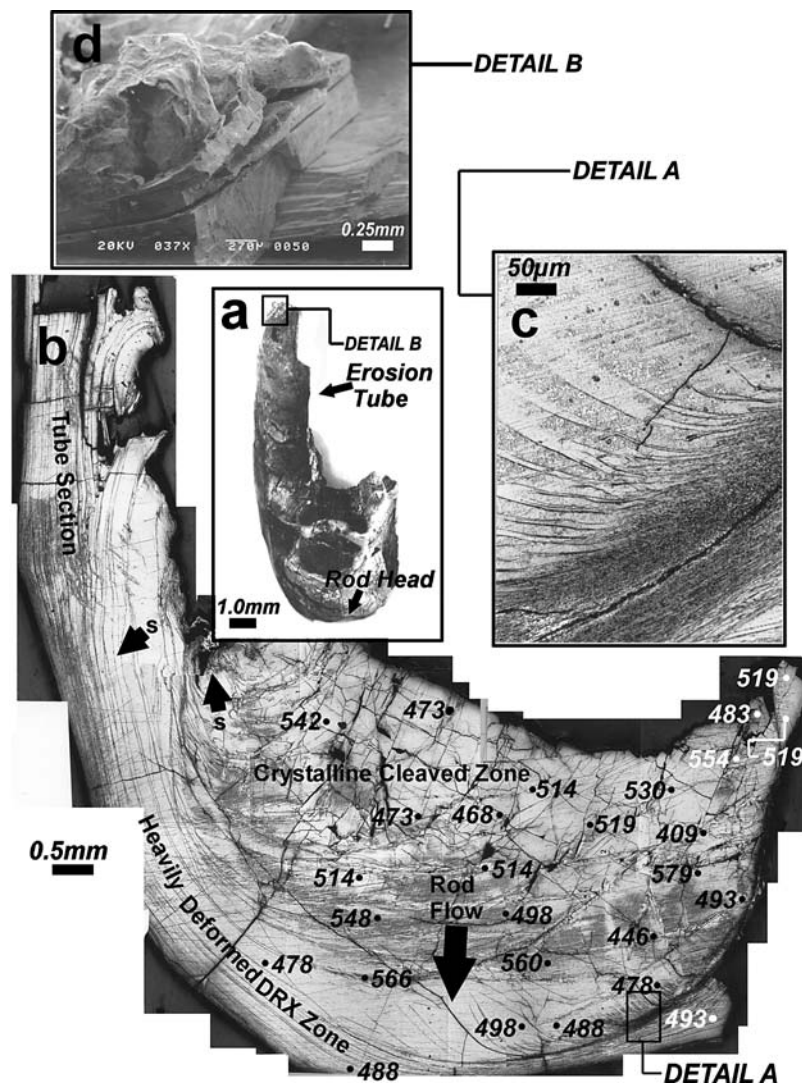

Figure 9 Macrograph of a W-5%Ta ZM-formed residual head and tube fragment obtained from shot ID#4 (Table I) after penetration(a). (b) Cross-section view of the fragment showing Vickers microhardness number (VHN) values. (c) Magnified view showing flow zone composed of overlapping shear bands and DRX grains. (d) SEM image of the tube's extension illustrating wide layers of microstructure.

3.3. ZM-formed W-5%Ta, [001] oriented single crystal residual fragments

Fig. 9a illustrates a ZM-formed W-5%Ta residual head and partial tube fragment obtained from shot ID #4 (Table I) after penetration. The cross-section view in Fig. 9b shows long, well-defined, overlapping adiabatic shear bands extending from the head of the penetrator, and terminating as part of the tube-like feature as indicated by arrows. Fig. 9d (detail *B*) is an SEM image obtained from the tube's extension, and illustrates wide, overlapping shear bands (or flow layers) of equiaxed, refined DRX microstructures similar to those shown in Figs 5 and 6. Such long, characteristic flow-features seem to reflect the improved ductility of the alloy (W-5%Ta) and therefore its ability to erode along the channel wall creating the long, contiguous tube. In contrast to the cross-section view in Fig. 8 (ZM-W), Fig. 9 (ZM-W-5%Ta) demonstrates the flow-induced deformation of the penetrating head to be more elongated and slender. Although a more fluid-dynamic head (Fig. 9) might seem ideal for penetration, the increased erosion along the channel wall (tube erosion in Fig. 3) diminishes the overall mass, and therefore reduces the momentum of the penetrating (rod) projectile. Consequently, as corroborated in previous studies, the addition of Ta is neither sufficient nor applicable in improving solid-state flow during penetration. In the case of the less ductile, pure tungsten material (Fig. 8b), the flow- characteristics seem to be shorter and thicker as indicated by the arrows labeled DRX in Figs 8c and d. The head is mushroom shaped due to the deformation mode which is less ductile and/or the lack of overlapping shear bands formed along the surface of the head (along the "Heavily Deformed Zone" in Fig. 8c and d). Due to this mushrooming of the head, the penetration channel cross-section area increases, ultimately diminishing the depth of penetration.

Flow-induced characteristic similarities between the two types of alloys (ZM-W and W-5%Ta) also exist. Vickers microhardness (VHN) mappings substantiate the existence of a well-defined, softer surface zone located at the head surface of the penetrator with a harder, cleaved zone behind. Fig. 9b exhibits a shear flow band composed of dynamically recrystallized (DRX) grains bordering the two distinct zones which is consistent with both tungsten CVD and ZM grown fragments, as shown in the magnified view in Fig. 9c. Also consistent with previous findings, a highly localized strain region located specifically on the top left side of the head similar to Fig. 8c) indicated by arrow (s), shows that the major flow activity (erosion from head to tube) might occur at distinct locations within the penetrator as illustrated schematically in Fig. 3 (at "s").

The cross-section view in Fig. 10a was obtained from the trailing tube end shown in Fig. 9a, and depicts flow features that are characteristic of the W-5%Ta rod penetrators (long, wide overlapping shear bands). The Vickers microhardness values shown in Fig. 10a also represent a harder tube region which corresponds to the characteristic microstructure. Al-
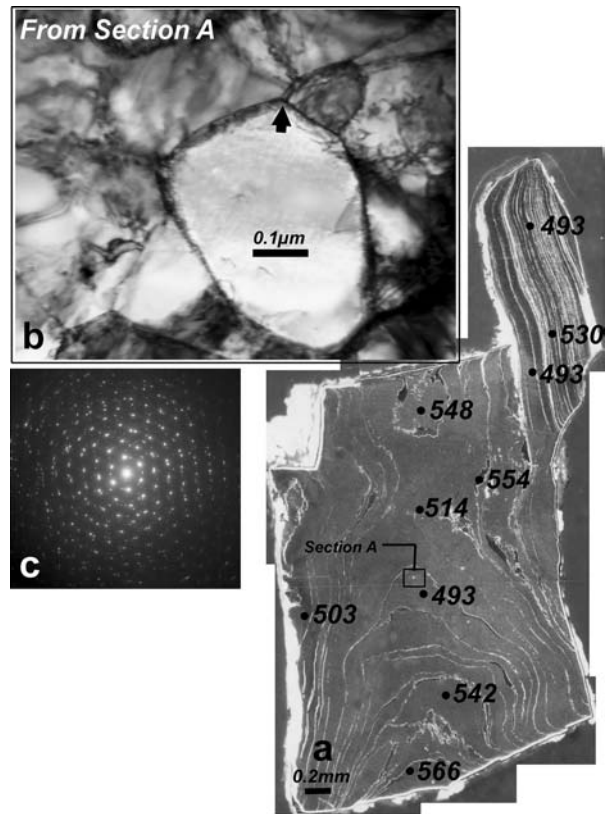

Figure 10 Cross-section view of a W-5% Ta-ZM residual tube extension obtained from shot ID#4 (Table I) Fig. 8(a). Vickers microhardness values are indicated in (a). (b) TEM image obtained from section A shown. Arrow indicates a triple junction of grain boundaries characteristic of well formed, recrystallized grain structure. (c) SAED pattern for (b).

though the microstructure is not observable with OM, TEM views reveal small, essentially equiaxed grain structures as seen in Fig. 10b. This type of microstructure is consistently present in all samples studied, including Figs 2a and 4c which were W-CVD grown projectile fragments. Fig. 10c indicates that the equiaxed, DRX grain structures shown in Fig 10b can represent both low and high-angle grain boundaries shown at the triple point indicated by the arrow in Fig. 10b.

4. Conclusions

Besides the initial microhardness difference, no observable variations between CVD and ZM-grown, W long-rod ballistic penetrators were found. Consequently, no difference in DRX efficiency between these specific growth methods (CVD and ZM) was observed. The addition of Ta seemed to improve the ductility of the W, and the flow of the ZM-W-5% Ta penetrator. Penetration depth appears to depend not only on projectile flow but also on the optimization and/or efficiency of DRX and shear banding as well because this controls the rate of erosion and the mushrooming of the head. This changes the penetration channel size and the overall efficiency of penetration.

Microstructural features, including deformation twins, adiabatic shear bands, and the overall occurrence

of DRX in both the penetrator head and tube were confirmed. Consistentwith prior studies, large equiaxed DRX grains were very prevalent in the tube section of the penetrator indicating residual grain growth during penetration. Evidence of a head surface zone which is believed to consist of heavily deformed DRX material was observed in dark-field OM views, and was then confirmed by residual microhardness values to be a softer zone. Peripherally along both sides of the penetrator head (high strain points), the DRX zone is followed by an adiabatic shear band or nucleating bands allowing flow and erosion to occur between this surface zone and the rod head center. These high strain points create a flow characteristic which seems to indicate a vortex-like effect creating a hot zone characterized by large, equiaxed grains. Within the rod head center, flow can occur by thin DRX sheets which are located between large crystalline, heavily deformed and cleaved blocks. Future studies, directed at characterizing and identifying these distinct zones within the residual penetrator head, embedded in the target, will allow for a better understanding of the penetration process, and the role played by the thin (0.5 mm) head regime which seems to have a different microstructure, with increasing flow features, when tantalum is added to [001] W.

References

1. L. E. MURR, H. K. SHIH and C-S. NIOU, *Mater. Charact.* **33** (1994) 65.
2. L. E. MURR, Y. LI, R. D. FLORES, E. A. TRILLO and J. C. MC CLURE, *Mater. Res. Innov.* **2**(3) (1998) 150.
3. S. A. QUINONES and L. E. MURR, *Phys. Stat. Sol.* (a) **166** (1998) 763.
4. S. PAPPU, S. SEN, L. E. MURR, D. KAPOOR and L. S. MAGNESS, *Mater. Sci. Engng.* **A298** (2001) 144.
5. E. A. TRILLO, E. V. ESQUIVEL, L. E. MURR and L. S. MAGNESS, *Mater. Character.* **48** (2002) 407.
6. L. E. MURR, E. A. TRILLO, S. PAPPU and C. KENNEDY, *J. Mater. Sci.* **37** (2002) 3337.
7. L. E. MURR and E. V. ESQUIVEL, *J. Mater. Sci.* **39** (2004) 1153.
8. E. V. ESQUIVEL, L. E. MURR, E. A. TRILLO and D. A. MARTINEZ, *Powder Met.* **46**(2) (2003) 137.
9. C. KENNEDY and L. E. MURR, *Mater. Sci. Engng.* **A325** (2002) 131.
10. L. E. MURR, E. FERREYRA, S. PAPPU, E. P. GARCIA, J. C. SANCHEZ, W. HUANG, J. M. RIVAS, C. KENNEDY, A. AYALA and C-S. NIOU, *Mater. Character.* **37** (1996) 245.
11. L. S. MAGNESS, JR., *Mech. Mater.* **17** (1994) 147.
12. W. J. BRUCHEY, E. J. HORWATH and P. W. KINGMAN, in "Tungsten and Tungsten Alloys—Recent Advances," edited by A. Crowson and E. Chen (TMS, Warrendale, PA, 1991) p. 121.
13. P. W. KINGMAN and R. A. HERRING, Ballistic penetration phenomenology of high symmetry single crystals. Report ARL-TR-700 (U.S. Army Research Laboratory, Aberdeen Proving Ground, MD, 1995).
14. W. LEONARD, L. S. MAGNESS, JR., R. W. DOWDING, J. TROGOLO, M. CHUNG and D. KAPOOR, in "Tungsten and Refractory Metals," edited by A. Bose and R. Dowding (TMS, Warrendale, PA, 1995) p. 149.
15. F. I. GRACE, in "Metallurgical and Materials Applications of Shock-Wave and High-Strain-Rate Phenomena," edited by L. E. Murr, K. P. Staudhammer and M. A. Meyers (Elsevier Science, B.V., Amsterdam, 1995) chap. 62, p. 521.